Mechanistic Insight into Dendrite-SEI Interactions for Lithium Metal Electrodes

Journal:	*Journal of Materials Chemistry A*
Manuscript ID	TA-ART-08-2018-007997.R1
Article Type:	Paper
Date Submitted by the Author:	12-Sep-2018
Complete List of Authors:	Hao, Feng; Purdue University, School of Mechanical Engineering Verma, Ankit; Purdue University, School of Mechanical Engineering Mukherjee, Partha; Purdue University, School of Mechanical Engineering

Mechanistic Insight into Dendrite-SEI Interactions for Lithium Metal Electrodes

Feng Hao, Ankit Verma, and Partha P. Mukherjee[*]

School of Mechanical Engineering, Purdue University, West Lafayette, IN 47907, USA

A revised manuscript submitted to

Journal of Materials Chemistry A

September 2018

---

[*] Email: pmukherjee@purdue.edu

Abstract

Solid electrolyte interphase (SEI) layer stability and homogeneity are critical toward understanding the root causes behind performance decay and safety concerns with lithium metal electrodes for energy storage. This study focuses on deducing mechanistic insights into the complexations between Li metal electrode and SEI during electrodeposition. It is found that the formation of Li dendrite can be initiated by two distinct mechanisms: (i) aggressive Li-ion depletion near the anode-SEI interface at high reaction rates or low temperature attributed to transport limitations, and (ii) spatially varying reaction kinetics at the SEI-electrode interface due to SEI inhomogeneity even at low currents. Subsequent mechanical stability analyses reveal that significantly high stress is generated due to nonuniform Li electrodeposition which could lead to crack formation in the existing SEI layer, and consequently exposure of fresh lithium to the electrolyte resulting in enhanced capacity fading. Furthermore, a non-dimensional analysis relating the interfacial stress induced failure propensity to electrochemical Biot number and SEI heterogeneity factor is proposed, which delineates stable lithium deposition regimes.

Keywords: Lithium metal electrode, Lithium electrodeposition, Solid electrolyte interphase, SEI heterogeneity, Interfacial stress

Introduction

Lithium metal as a negative electrode has attracted tremendous interest due to the burgeoning demand for electrical energy storage.[1-3] Universally considered in the scientific community as the "Holy Grail" anode, Li metal surpasses current commercial Li-ion intercalation anodes with regards to specific gravimetric capacity (~3862 mAh/g for Li metal vs. 372 mAh/g for graphite), low density (~0.534 g/cm^3 for Li metal vs. ~2.2 g/cm^3 for graphite), and the lowest negative electrochemical potential (0 V vs. Li/Li$^+$ for Li metal against stoichiometrically varying 0 - 1.5V vs. Li/Li$^+$ for graphite).[4, 5] Consequently, Li metal offers a realistic perspective for high energy density rechargeable batteries; also evidenced by the resurgent research focus in beyond Li-ion chemistry, such as Li-sulfur and Li-air battery systems.[6-8] A critical challenge for Li metal anodes centers around unmitigated Li dendrite growth, which degrades cell performance and causes safety concerns, such as low cycling efficiency, thermal runaway, and short circuit.[9-11] Several approaches have been proposed to enable dendrite-free electrodeposition, for example, utilizing solid electrolytes with high toughness to prevent dendrite propagation,[12-14] employing highly concentrated electrolytes to prevent electrolyte depletion,[15] and electrolyte additives to slow dendrite growth kinetics,[16, 17] as well as patterning nano/microscale electrolyte transport channels to regulate Li-ion flux distribution,[18-20] amongst other techniques.[21-23]

A common feature of intercalation (such as, graphite) and Li metal anodes for liquid electrolyte systems is the formation of a passivating layer known as the solid electrolyte interphase (SEI) through the reduction of electrolyte solvent and salt with Li, intercalated or otherwise. The

SEI layer allows for the transport of Li-ion from the electrolyte to the anode surface while preventing further deleterious reactions between the anode and electrolyte.[24-27] The mechanism of SEI formation in intercalation anodes (e.g., graphite) is well established; SEI is predominantly formed during the initial formation cycles, growing continuously with further electrochemical cycling, albeit at a much slower rate, which contributes to the capacity fade of the Li-ion battery system.[28, 29] For state-of-the-art Li metal anode, extensive efforts have been made to unravel the SEI formation mechanisms.[23, 30-32] Similar to the case of graphite, the SEI on Li anode is multicomponent, of which the major inorganic constituents include Li_2O, Li_2S/Li_2S_2, LiF, Li_2CO_3, and LiOH, depending on the battery system and operating conditions.[30]

For commercially used intercalation anodes (e.g., graphite), the SEI exhibits good chemical and mechanical stabilities under small volumetric changes (~10%) of the active material.[33] In contrast, the immense volume change of Li metal renders the SEI unstable, eventually resulting in disintegration of the SEI layer. The fracture of the SEI layer decreases local Li-ion transfer resistance, thereby initiating Li dendrite formation.[34] Also, repetitive fracture of the SEI during Li plating/stripping results in fresh contact of electrolyte with Li metal surface, resulting in unabated parasitic Li depleting reduction reactions leading to faster SEI growth and poor cycling efficiency.[5] Additionally, an inhomogeneous SEI layer can induce Li dendrite formation due to the spatially non-uniform Li-ion flux through the SEI. Therefore, it is imperative to develop fundamental understanding of the lithium metal and SEI interactions.

In the field of electrodeposition, the growth mechanism of metallic electrodeposits has been examined theoretically in literature. For instance, the dendrite tip is found to have a faster deposition rate stemming from spherical diffusion.[35] Nevertheless, theoretical studies are lacking with respect to the role of SEI during initial Li nucleation and growth. In literature, it has been proposed that SEI can break down while accommodating the morphological changes of the Li metal surface.[4, 34] In this regard, we aim to develop a mechanistic understanding of the lithium electrodeposition and SEI interactions based on a mesoscale formalism, especially focusing on the inhomogeneity of the SEI layer. Lithium dendrite induced mechanical instability of the SEI layer is further examined. To simplify the complexity of modeling coupled Li deposition and SEI electrochemical reactions, as a first approximation, the electrochemical details of the SEI growth during Li electrodeposition is not considered.[29]

Results and discussion

1. Impact of deposition reaction kinetics and temperature with homogeneous SEI

For Li plating, the related model is illustrated in Figure 1(a), which shows the three processes considered in this study. In the vicinity of the SEI layer, lithium ion sheds its solvent molecules and resides on the SEI layer upper surface. Subsequently, the Li ion diffuses through the SEI layer. Upon the arrival at the Li metal-SEI interface, the Li-ion is reduced and then directly deposited on the Li metal surface, accompanied by the electron transfer. As the electrodeposition continues, the accumulated Li drives the Li-SEI interface evolution (i.e., moving upward). In this study, the SEI thickness is assumed to be 21 nm, which is consistent with the reported ones in literature.[30, 36, 37]

To begin with, a homogeneous SEI layer is considered to study Li electrodeposition on the lithium metal anode. Initially, the flat SEI layer is in perfect contact with Li metal. The operating temperature is maintained at 300 K. To quantify the roughening of Li metal-SEI interface, the roughness parameter is formulated as:

$$R_a = \frac{1}{L}\int_0^L \left|x - x_c\right| \mathrm{d}y, \tag{1}$$

where R_a is referred to as the arithmetical averaged deviation of the assessed profile, x is the vertical distance from the mean line, x_c is the height of the mean line, and y is the corresponding position in the horizontal direction.

Figure 1(b) shows the roughness of Li metal-SEI interface as a function of the overpotential. For instance, R_a is 0.8 nm for the deposition morphology at the overpotential of 0.18 V exhibiting uniform film type deposits. As the overpotential increases, the Li metal surface becomes rough at the nanoscale during Li plating, showing a series of peaks and troughs with dimensional variability. Roughness increases with the local overpotential and shows an exponential increase when the overpotential exceeds 0.22 V. Eventually, the drastic change in the roughness of the undulating Li metal-SEI interface leads to the formation of Li dendrite. In this case (T = 300 K), Li dendrite is initiated at the overpotential of 0.24 V. High deposition overpotential results in high plating current density favoring Li dendrite formation, and transport limitations become prominent. Thus, Li metal is prone to form dendrites under high current density, which has also been rationalized in earlier studies.[38]

In addition to overpotential, temperature also affects Li electrodeposition. In terms of local overpotential and temperature, Figure 1(c) depicts the phase map for Li deposition morphology, which is divided into two categories: uniform deposition (green) and dendrite (yellow). For a given overpotential, Li is uniformly deposited over the anode surface at high temperatures. However, as the temperature decreases, the morphology can experience a transition from film-type Li deposits to Li dendrite. According to Equation (3), Li-ion diffusion rate in the SEI is reduced as the temperature goes down, and thus, sluggish Li-ion transport in the SEI primarily accounts for Li dendrite growth at relatively low temperatures. From experiments, the initiation time of Li dendrite was observed to be shortened at a low temperature,[39] and a theoretical model also found that Li dendrite formation was favored at a low temperature.[40]

To further explore Li plating behavior, theoretical analysis is used to understand the mechanism of Li dendrite formation. For the system considered here, the limiting current density is given as

$$i_L = \frac{2c_0 DF}{h}, \tag{2}$$

where c_0 is the initial bulk concentration of Li-ions in the SEI (1.5 M), h is the thickness of SEI (21 nm), and the SEI diffusivity D can be obtained by[41]

$$D = d^2 \nu \exp\left(-\frac{E_a}{k_b T}\right), \tag{3}$$

where d is the distance between two adjacent sites, i.e. 3.5 Å. Using the parameters listed in Table 1, the calculated diffusivity of Li-ion in SEI is 4.7×10^{-10} cm^2/s, which is much smaller than the reported ones in liquid electrolytes,[42] but comparable to Li diffusivities in insertion-host electrode materials.[43-45] Using Equation (5), we get the limiting current density as 64.8 mA cm^{-2}. Theoretically, i_L is the maximum current density that the electrochemical system can achieve.

Figure 2(a) shows the current density profiles at varying overpotentials, where the total time, t_M is estimated as 1.03 s, 0.32 s, and 0.16 s for the overpotentials of 0.12 V, 0.18 V, and 0.25 V, respectively. In the early stage of Li plating, the current density rapidly increases as the SEI is filled with Li-ions. For the overpotentials of 0.12 V and 0.18 V, the current densities reach relatively stable values. In contrast, the overpotential of 0.25 V leads to an unstable current density, which gradually approaches to the critical current density i_L. Under this situation, the enhanced roughening of Li metal-SEI interface contributes to the formation of Li dendrites.

Correspondingly, Figure 2(b) shows Li-ion concentration profiles in the SEI thickness direction, which compares results from the kinetic model (scatter) and theoretical prediction (line). The steady-state concentration distribution for the system under study can be analytically obtained as (Supplementary Information):

$$\frac{c}{c_0}=\frac{i}{i_L}\left(1-2\frac{x}{h}\right)+1. \tag{4}$$

From Figure 2(a), the theoretically predicted critical current density of Li dendrite formation is consistent with the one in the kinetic model, and the concentration distributions from the analytical solution are also in good agreement with those based on the kinetic model in Figure 2(b). It is to be noted that both the kinetic model and analytical estimation demonstrate complete Li-ion depletion at the Li metal-SEI interface when Li dendrite is initiated.

2. SEI heterogeneity implications

It should be noted that the aforementioned results are obtained under the assumption that SEI layer is homogeneous. In reality, SEI exhibits a complex structure, comprising various components, and the resulting spatial heterogeneity can affect Li-ion transport and reduction at the Li metal surface. To study the effect of the SEI layer inhomogeneity, the center region of SEI is assigned a different diffusivity D_c, varied by changing the Li-ion diffusion barrier in the SEI (see Table 2S in Supplementary Information). Hence, D_c/D represents the SEI inhomogeneity in our model. For the subsequent results, the dimensions of the center region are set to 0.1 L (L the system length) by h (h the SEI height), the operating temperature is 300 K, and the overpotential is 0.15 V, which produces a current density around 0.3 i_L, much smaller than the limiting current density i_L.

Figures 3(a)-(c) illustrate Li deposition morphologies for $D_c/D = 1$, $D_c/D = 3.2$, and $D_c/D = 0.3$, respectively from the numerical model. Here, grey is SEI, blue is Li metal, and red is Li-ion. In the three cases shown, only the diffusivity in the center region is varied. The three snapshots are captured at the same time of 0.12 s. In Figure 3(a), because of the homogeneous SEI, Li-ion is uniformly distributed in the length direction, leading to uniform Li deposition over the anode surface. The central region with disparate diffusivity is highlighted in light blue in Figures 3(b) and 3(c). From Figure 3(b), it is evident that that more Li-ions are reduced and deposited in the center region due to its relatively larger diffusivity. As a result, needle-like Li begins to grow. Here, it implies that owing to the inhomogeneity, Li dendrite can be initiated even if the current density is much smaller than the limiting current density, i.e. $i = 0.3\ i_L$. This result is in good agreement with the reported experiments, where Li dendrite could be observed even at low rates.[4, 46, 47] Conversely, Figure 3(c) shows that fewer Li-ions are deposited in the center region ($D_c/D = 0.3$) compared to other locations, thereby forming a cavity at the center.

Figure 3(d) shows Li-ion concentration profiles in the length direction, where the center region has a lower diffusion barrier. It can be seen that a peak arises at the center, where Li-ion concentration becomes larger as D_c/D increases. In addition to Li-ion flux in the thickness direction, local Li-ion flux is formed near the center region shown in Figure 3(b), and thus, Li-ions are attracted into the center region from outside. As a result, the center region is replenished with more Li-ions to support the growth of Li dendrite. Figure 3(d) also indicates that because of the local flux, relatively low Li-ion concentration is caused on the adjoining sides of the center region. Conversely, Figure 3(e) shows that the center region has the minimum Li-ion concentration. Li-ions exhibit tendency to diffuse from the center region to outside, which leads to elevated Li-ion concentration in the region adjacent to the center region. Figure 3 demonstrates that the inhomogeneity in diffusivity dramatically affects Li-ion flux and thus Li electrodeposition morphology.

The aforementioned results strengthen the hypothesis that the presence of SEI inhomogeneity can lead to highly non-uniform lithium electrodeposition. The resulting dendrite/cavity formation can also generate stress in the SEI, which could affect the SEI layer stability and lead to performance decay. To analyze the mechanical stability of the SEI, Li plating induced stress in the SEI is examined by using finite element method. In our model, the periodic boundary condition is applied in the length direction (y-axis direction). In the thickness direction (x-axis direction), the displacement field of the SEI lower surface is determined by the roughness profile at the Li metal-SEI phase boundary. The SEI upper surface is assumed to be stress-free, implying that the resistance from the electrolyte to the growing Li anode is neglected, which is applicable to the system with liquid electrolytes before the deposited Li impinges onto the separator. For the mechanical properties of the SEI layer, the Young's modulus and Poisson's ratio are set to 10 GPa and 0.3, respectively.

Figure 4(a) shows the profile of Li metal-SEI interface for the case of $D_c/D = 3.2$ (higher center region diffusivity). The corresponding stress field in the SEI is illustrated in Figure 4(b), with the x-axis direction along the vertical direction and y-axis direction along the horizontal direction. Negative stress values indicate compressive stress and positive values imply tensile stress. For the stress in the x-axis direction σ_{xx}, the upper contour in Figure 4(b) shows that the center region is subject to large compressive stresses (dark blue) at Li metal-SEI interface, originating from the pressure induced by Li dendrite growth in the x-axis direction. To balance the compressive stress in the center region, the two sides adjacent to the center region undergo large tensile stresses. Different from the stress σ_{xx}, the contour of σ_{yy} indicates that the stress in the center region experiences a distinct transition from compressive to tensile stress signature initiating from the Li metal-SEI interface. In Figure 4(b), the interfacial roughness at other locations also generates stress, but the affected zone is much smaller than the one induced by the dendrite in the center region.

Figure 4(d) shows the stress field in the SEI under the profile of Li metal-SEI interface for the case of $D_c/D = 0.3$ (lower center region diffusivity) in Figure 4(c), with a cavity in the center region. Compared to the stresses in Figure 4(b), Figure 4(d) shows that most regions have relatively smaller stresses, which are of opposite sign. For example, σ_{yy} in the center region experiences an opposite transition from tensile stress to compressive stress in the thickness direction. From Figure 4, it can be seen that huge stresses mainly occur near the center region, where dendrites and cavities are formed. This stress could fracture the passivated SEI layer leading to the creation of fast Li-ion transport channels, and the large local Li-ion flux, in turn, favors Li dendrite growth at these "hot spots".[34] After the dendrite is exposed to fresh electrolyte, unabated SEI growth can occur resulting in capacity fade and poor cycling efficiency.[5]

3. Non-dimensional analysis of deposition stability

Further, the maximum shear stress is used to assess the mechanical stability of SEI, consistent with the Tresca yield criterion in failure theory.[48] In view of the large stress near the center region, the average maximum shear stress is calculated for the SEI bottom spanning 0.3 L, the center part (0.1 L) and the two sides of the center part (both 0.1 L). To delineate the impact of the coupled transport-reaction dynamics and the SEI inhomogeneity on stress generation, consistent non-dimensional numbers corresponding to each phenomenon are defined. We introduce the electrochemical Biot number, Bi_{echem}, contrasting the relative magnitudes of the Li-ion diffusive transport resistance in the SEI to the charge transfer resistance at the Li metal-SEI interface. This formulation is derived analogously from electrochemical Biot number formulation for intercalation electrode comparing the relative magnitudes of diffusive transport resistance of Li atoms inside the electrode particles and interfacial charge transfer resistance at the electrode particle-electrolyte interface. A large magnitude of the Biot number corresponds to diffusion-limited scenario, while small Biot number systems are dominated by the interfacial resistance. For the Li metal-SEI system, the electrochemical Biot number is defined as:

$$Bi_{echem} = \frac{ih}{c_o DF} \quad . \tag{5}$$

The diffusivity, D, used here is the nominal diffusivity of Li^-ions in the SEI, as defined earlier. SEI heterogeneity, χ, is quantified using the ratio of Li-ion diffusivities in the central and adjacent regions of the SEI

$$\chi = \frac{D_c}{D} \tag{6}$$

Figure 5 shows a contour map of the stress magnitude in the center region as a function of the electrochemical Biot number and SEI inhomogeneity. The results demonstrate that the maximum stress shows rapid increase with SEI inhomogeneity while it has a relatively weak dependence on the electrochemical Biot number, and correspondingly current density. For a fixed current density, increased SEI inhomogeneity facilitates the growth of Li dendrite. For a specific SEI heterogeneity, the growth of Li dendrite also shows direct correlation with current density increase. The simultaneous increase of current density and SEI heterogeneity has a compounding effect, causing large stresses which leads to the breakdown of SEI when the stress reaches the yield strength in shear. Thus, SEI heterogeneity can aggravate dendrite formation and cause SEI disintegration even at current densities far below the limiting current densities. It is evident that stability of electrodeposition and SEI layer is favored under low electrochemical Biot number operation with homogenous SEI characteristics. Furthermore, a mechanically robust SEI can alleviate the failure caused by Li growth during plating. SEI with a higher yield stress can endure uneven Li electrodeposition due to a higher current density or a higher SEI inhomogeneity, which inhibits crack formation in SEI and thus averts parasitic reactions between electrolyte and Li electrode, thereby enhancing capacity retention.

The results shown here suggest that the formation of Li dendrite can be initiated under significantly high overpotential and/or low operating temperature, as the current density approaches the limiting current density. According to Equation (5), it can be concluded that Li dendrite can be suppressed by increasing Li-ion concentration and improving Li-ion diffusion kinetics in the SEI. Because of the SEI inhomogeneity, non-uniform Li-ion flux can result in Li dendrite formation even if the current density is significantly lower than the limiting current density. The formation of dendrites and cavities generate large stresses at the Li metal-SEI interface. This may lead to performance decay due to the mechanical instability of the SEI layer with cycling. For lithium metal anodes, suppressing Li dendrite is critical in ensuring cyclability, which is partly governed by the SEI homogeneity. In the future, this study will be extended to describe concurrent SEI growth and Li electrodeposition for lithium metal anodes.[29, 49]

Conclusion

In summary, we investigated the role of reaction kinetics, operating temperature and SEI inhomogeneity on Li electrodeposition morphology alongside mechanical stability of the SEI layer. The kinetic model illustrated the mechanisms for transition of film-type deposition morphology to dendritic deposits at high reaction current densities and low operating temperatures for homogenous SEI. A steep increase in the SEI-Li interface roughness characterized this transition regime and is a direct consequence of Li-ion transport limitations in the electrolyte. The results also demonstrate the importance of SEI inhomogeneity; preferential deposition of Li metal occurs in SEI regions with rapid diffusion leading to Li dendrite formation, even at low current densities with no apparent transport limitations. Conversely, SEI regions with sluggish transport results in the evolution of deposit free cavities over the corresponding domain. Subsequent mechanics analyses revealed that the occurrence of preferential dendrites/cavities result in increased perturbations of the Li-SEI interface and localized stress ramps in the vicinity of the irregularities, which can rupture the SEI layer, as evidenced by the SEI stability phase map analysis based on electrochemical Biot number and SEI inhomogeneity. This work offers a fundamental mechanistic understanding of the effects of SEI on Li electrodeposition morphology, providing insights into the role of Li plating-SEI interactions in battery degradation.

Computational method

For lithium metal anodes, the principal electrochemical reaction on the anode surface is $Li^+ + e \leftrightarrow Li$. Here, the local faradaic current density generated by the reaction is described by the Butler-Volmer equation:[50]

$$i_R = i_0\left(\exp\left(\frac{\alpha F}{RT}\eta\right) - \exp\left(-\frac{\beta F}{RT}\eta\right)\right). \tag{7}$$

where i_0 is the exchange current density of the redox reactions on Li metal, which could be as large as 2 to 5 mA/cm.[51, 52] Here, α and β are the charge transfer coefficients, obeying the relation, $\alpha + \beta = 1$, F is the Faraday's constant, R is the gas constant, and T is the operating temperature. η is the overpotential, which is the driving force for the electrochemical reactions.

For a single lattice site at the Li metal-SEI interface, the reaction rate is thus expressed as:

$$k_J = \left\{0,\ \frac{i_R a^2}{F} N_a\right\}, \tag{8}$$

where a is the lattice constant of crystallized Li, and N_a is the Avogadro constant. It should be noted that when no Li ion is present at an interfacial site, the local reaction rate is zero.

Li-ion transport in the SEI layer is assumed to obey the Arrhenius expression:[41]

$$k = \nu \exp\left(\frac{-E_a}{k_b T}\right), \tag{9}$$

where v is the pre-exponential factor, approximately 10^{12}~10^{13} s^{-1}, k_b is the Boltzmann constant, and E_a is the energy barrier that needs to be overcome for Li-ion diffusion through SEI.

An account of the simplifying assumptions in the model is given here. The lattice size is 3.5 Å, which is the same as that of bulk Li.[53] Since a unit cell of Li contains two Li atoms, two adjacent Li-ions are assumed to be reduced concurrently, which indicates that one lattice site in the anode domain represents a unit cell of Li. For the two-dimensional model, the system has a length of 70 nm (L) and a height of 70 nm (H), composed of a 200×200 grid of 40000 lattice sites. SEI has a size of 70 nm (L) by 21 nm (h). In the length direction, the periodic boundary condition is applied. In the SEI domain, Li-ion concentration is kept at 1.5 M (M = 1000 mol/m^3), which is equivalent to 2% of the sites in the SEI being occupied by Li-ions. To compensate Li consumption at the Li metal-SEI interface, new Li-ions are therefore adsorbed to the SEI upper surface, as shown in Figure 1(a). The calculation runs until 7600 Li atoms are deposited on the anode surface. More details of our methods are provided in Supplementary Information, including dynamical evolution during Li plating, parameters used in the kinetic model, theoretical analysis of Li-ion concentration distribution, and stress analysis.

Conflicts of interest

There are no conflicts to declare.

Acknowledgements

The information, data, or work presented herein was funded in part by the Office of Energy Efficiency and Renewable Energy (EERE), U.S. Department of Energy, under Award DE-EE0007766.

References

1. D. Larcher and J. M. Tarascon, *Nature Chemistry*, 2014, **7**, 19.
2. W. Xu, J. Wang, F. Ding, X. Chen, E. Nasybulin, Y. Zhang and J.-G. Zhang, *Energy & Environmental Science*, 2014, **7**, 513-537.
3. J. W. Choi and D. Aurbach, 2016, **1**, 16013.
4. K. N. Wood, M. Noked and N. P. Dasgupta, *ACS Energy Letters*, 2017, **2**, 664-672.
5. D. Lin, Y. Liu and Y. Cui, *Nature Nanotechnology*, 2017, **12**, 194.
6. Z. Liu and P. P. Mukherjee, *ACS Applied Materials & Interfaces*, 2017, **9**, 5263-5271.
7. Z. Liu, S. Bertolini, P. B. Balbuena and P. P. Mukherjee, *ACS Applied Materials & Interfaces*, 2016, **8**, 4700-4708.
8. G. Girishkumar, B. McCloskey, A. C. Luntz, S. Swanson and W. Wilcke, *The Journal of Physical Chemistry Letters*, 2010, **1**, 2193-2203.
9. F. Wu, Y.-X. Yuan, X.-B. Cheng, Y. Bai, Y. Li, C. Wu and Q. Zhang, *Energy Storage Materials*, 2018, **15**, 148-170.
10. S. S. Zhang, *ACS Applied Energy Materials*, 2018, **1**, 910-920.
11. K.-H. Chen, K. N. Wood, E. Kazyak, W. S. LePage, A. L. Davis, A. J. Sanchez and N. P. Dasgupta, *Journal of Materials Chemistry A*, 2017, **5**, 11671-11681.
12. K. Kerman, A. Luntz, V. Viswanathan, Y.-M. Chiang and Z. Chen, *Journal of The Electrochemical Society*, 2017, **164**, A1731-A1744.
13. P. Barai, K. Higa and V. Srinivasan, *Physical Chemistry Chemical Physics*, 2017, **19**, 20493-20505.
14. D. T. Hallinan, S. A. Mullin, G. M. Stone and N. P. Balsara, *Journal of The Electrochemical Society*, 2013, **160**, A464-A470.
15. S. Chen, J. Zheng, D. Mei, K. S. Han, M. H. Engelhard, W. Zhao, W. Xu, J. Liu and J.-G. Zhang, *Advanced Materials*, 2018, **30**, 1706102.
16. F. Ding, W. Xu, G. L. Graff, J. Zhang, M. L. Sushko, X. Chen, Y. Shao, M. H. Engelhard, Z. Nie, J. Xiao, X. Liu, P. V. Sushko, J. Liu and J.-G. Zhang, *Journal of the American Chemical Society*, 2013, **135**, 4450-4456.
17. R. Miao, J. Yang, X. Feng, H. Jia, J. Wang and Y. Nuli, *Journal of Power Sources*, 2014, **271**, 291-297.
18. X.-B. Cheng, T.-Z. Hou, R. Zhang, H.-J. Peng, C.-Z. Zhao, J.-Q. Huang and Q. Zhang, *Advanced Materials*, 2016, **28**, 2888-2895.
19. Y. Zhang, W. Luo, C. Wang, Y. Li, C. Chen, J. Song, J. Dai, E. M. Hitz, S. Xu, C. Yang, Y. Wang and L. Hu, *Proceedings of the National Academy of Sciences*, 2017, **114**, 3584-3589.
20. S.-H. Wang, Y.-X. Yin, T.-T. Zuo, W. Dong, J.-Y. Li, J.-L. Shi, C.-H. Zhang, N.-W. Li, C.-J. Li and Y.-G. Guo, *Advanced Materials*, 2017, **29**, 1703729.

21. K. Yan, Z. Lu, H.-W. Lee, F. Xiong, P.-C. Hsu, Y. Li, J. Zhao, S. Chu and Y. Cui, *Nature Energy*, 2016, **1**, 16010.
22. R. Khurana, J. L. Schaefer, L. A. Archer and G. W. Coates, *Journal of the American Chemical Society*, 2014, **136**, 7395-7402.
23. X.-B. Cheng and Q. Zhang, *Journal of Materials Chemistry A*, 2015, **3**, 7207-7209.
24. E. Peled, D. Golodnitsky and G. Ardel, *Journal of The Electrochemical Society*, 1997, **144**, L208-L210.
25. X. Yu and A. Manthiram, *Accounts of Chemical Research*, 2017, **50**, 2653-2660.
26. P. Verma, P. Maire and P. Novák, *Electrochimica Acta*, 2010, **55**, 6332-6341.
27. S. Shi, P. Lu, Z. Liu, Y. Qi, L. G. Hector, H. Li and S. J. Harris, *Journal of the American Chemical Society*, 2012, **134**, 15476-15487.
28. M. B. Pinson and M. Z. Bazant, *Journal of The Electrochemical Society*, 2013, **160**, A243-A250.
29. F. Hao, Z. Liu, P. B. Balbuena and P. P. Mukherjee, *The Journal of Physical Chemistry C*, 2017, **121**, 26233-26240.
30. X.-B. Cheng, R. Zhang, C.-Z. Zhao, F. Wei, J.-G. Zhang and Q. Zhang, *Advanced Science*, 2016, **3**, 1500213-n/a.
31. G. Bieker, M. Winter and P. Bieker, *Physical Chemistry Chemical Physics*, 2015, **17**, 8670-8679.
32. K. Leung, F. Soto, K. Hankins, P. B. Balbuena and K. L. Harrison, *The Journal of Physical Chemistry C*, 2016, **120**, 6302-6313.
33. M. Hahn, H. Buqa, P. W. Ruch, D. Goers, M. E. Spahr, J. Ufheil, P. Novák and R. Kötz, *Electrochemical and Solid-State Letters*, 2008, **11**, A151-A154.
34. D. Aurbach, *Journal of Power Sources*, 2000, **89**, 206-218.
35. J. L. Barton and J. O'M. Bockris, *Proceedings of the Royal Society of London. Series A. Mathematical and Physical Sciences*, 1962, **268**, 485-505.
36. P. Lu and S. J. Harris, *Electrochemistry Communications*, 2011, **13**, 1035-1037.
37. E. Peled and S. Menkin, *Journal of The Electrochemical Society*, 2017, **164**, A1703-A1719.
38. J. N. Chazalviel, *Physical Review A*, 1990, **42**, 7355-7367.
39. C. T. Love, O. A. Baturina and K. E. Swider-Lyons, *ECS Electrochemistry Letters*, 2015, **4**, A24-A27.
40. R. Akolkar, *Journal of Power Sources*, 2014, **246**, 84-89.
41. A. Urban, D.-H. Seo and G. Ceder, *Npj Computational Materials*, 2016, **2**, 16002.
42. L. O. Valøen and J. N. Reimers, *Journal of The Electrochemical Society*, 2005, **152**, A882-A891.
43. J. Christensen and J. Newman, *Journal of The Electrochemical Society*, 2006, **153**, A1019-A1030.

44. P. Yu, B. N. Popov, J. A. Ritter and R. E. White, *Journal of The Electrochemical Society*, 1999, **146**, 8-14.
45. A. Verma, K. Smith, S. Santhanagopalan, D. Abraham, K. P. Yao and P. P. Mukherjee, *Journal of The Electrochemical Society*, 2017, **164**, A3380-A3392.
46. K. N. Wood, E. Kazyak, A. F. Chadwick, K.-H. Chen, J.-G. Zhang, K. Thornton and N. P. Dasgupta, *ACS Central Science*, 2016, **2**, 790-801.
47. H. J. Chang, A. J. Ilott, N. M. Trease, M. Mohammadi, A. Jerschow and C. P. Grey, *Journal of the American Chemical Society*, 2015, **137**, 15209-15216.
48. R. M. Christensen,*The theory of materials failure*, Oxford University Press, 2013.
49. F. Hao, A. Verma and P. P. Mukherjee, *ACS Applied Materials & Interfaces*, 2018, **10**, 26320-26327.
50. F. Hao and P. P. Mukherjee, *Journal of The Electrochemical Society*, 2018, **165**, A1857-A1864.
51. K. E. T.-A. J. Newman, *Electrochemical systems, John Wiley & Sons*, 2012.
52. P. Arora, M. Doyle and R. E. White, *Journal of The Electrochemical Society*, 1999, **146**, 3543-3553.
53. M. Jäckle and A. Groß, *The Journal of Chemical Physics*, 2014, **141**, 174710.

List of Figures

Figure	***Caption***
1	(a) Schematic of Li electrodeposition on lithium metal anode surface. Here, the red circles are Li-ions, the green circles are solvent molecules, and the blue is metallic Li. Reaction process: Li-ion desolvation from electrolyte to the top surface of SEI, Li-ion diffusion in the SEI layer, and Li deposition at the Li metal-SEI interface. (b) Nanoscale roughness of Li metal-SEI interface at various local overpotentials under the temperature of 300 K, with two representative interface morphologies inserted. (c) Phase map of Li electrodeposition morphology in terms of local overpotential and temperature. Dendritic deposition is observed at low temperatures and high overpotential.
2	(a) Current density profiles at varying overpotentials. Here i_L and t_M are the limiting current density and total deposition time. The total deposition times are 1.03 s (0.12 V), 0.32 s (0.18 V), and 0.16 s (0.25 V). Corresponding to the three cases, Li-ion concentration profiles are shown in (b). Here, the lines are theoretical prediction and symbols correspond to computations.
3	Effect of SEI inhomogeneity on Li electrodeposition. Here, the red circles are Li-ions and the blue circles are deposited Li atoms. Diffusion kinetics is varied in the center region, possessing a length of 0.1 L (L the system length) and a height of h (h the SEI height). (a) Homogeneous SEI. (b) The center region has a lower diffusion barrier. (c) The center has a higher diffusion barrier. (d) and (e) are the concentration profiles in the SEI layer obtained from the computational model.
4	Nonuniform electrodeposition induced stress in the SEI layer. (a) Profile of the Li metal-SEI interface with D_c/D = 3.2, and (b) the corresponding stress contours $\left(\sigma_{xx}, \sigma_{yy}\right)$ in SEI. (c) Profile of the Li anode-SEI interface with D_c/D = 0.3, and (d) the corresponding stress contours $\left(\sigma_{xx}, \sigma_{yy}\right)$ in the SEI layer.
5	Phase map for maximum shear stress (Tresca failure criteria) as a function of electrochemical Biot number $\left(Bi_{echem}\right)$ and SEI heterogeneity$\left(\chi\right)$. Maximum stress scales strongly with SEI inhomogeneity and shows mild increase with current density causing SEI fracture.

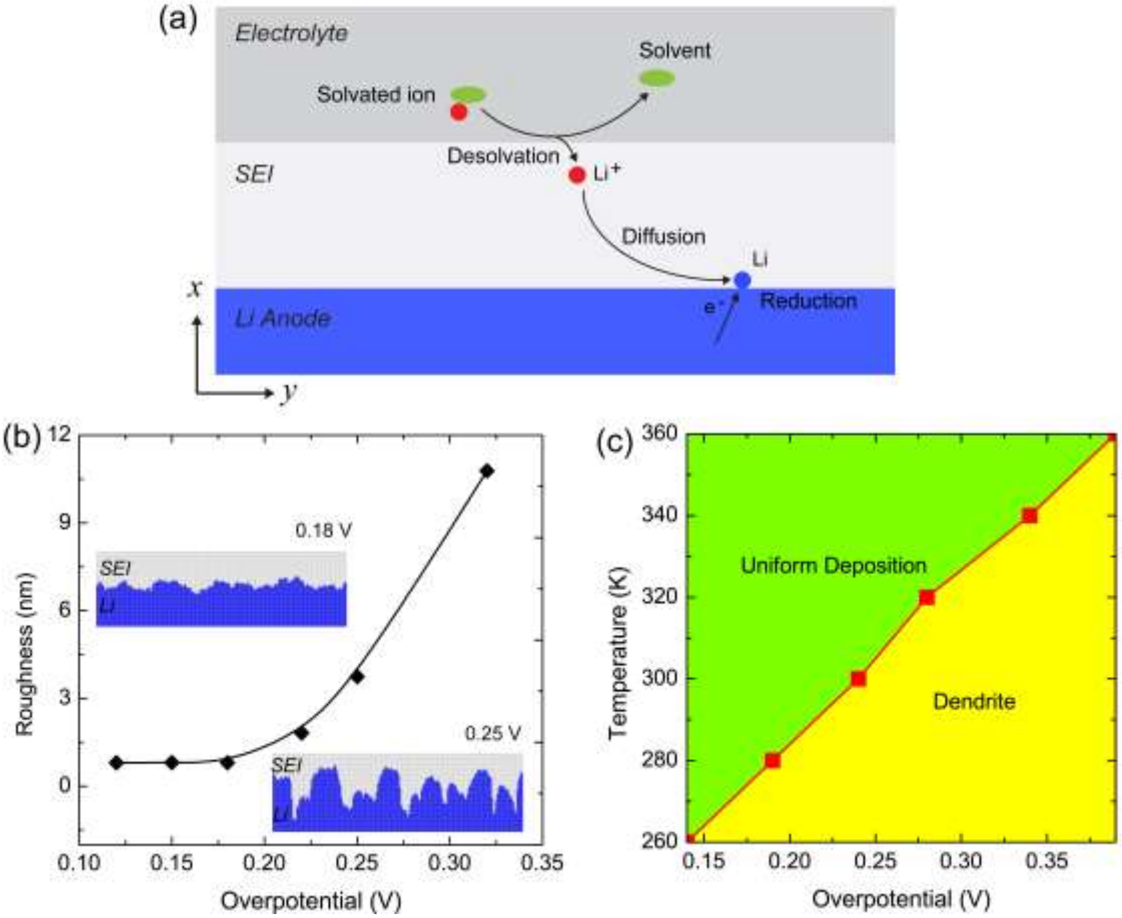

Figure 1. (a) Schematic of Li electrodeposition on lithium metal anode surface. Here, the red circles are Li-ions, the green circles are solvent molecules, and the blue is metallic Li. Reaction process: Li-ion desolvation from electrolyte to the top surface of SEI, Li-ion diffusion in the SEI layer, and Li deposition at the Li metal-SEI interface. (b) Nanoscale roughness of Li metal-SEI interface at various local overpotentials under the temperature of 300 K, with two representative interface morphologies inserted. (c) Phase map of Li electrodeposition morphology in terms of local overpotential and temperature. Dendritic deposition is observed at low temperatures and high overpotential.

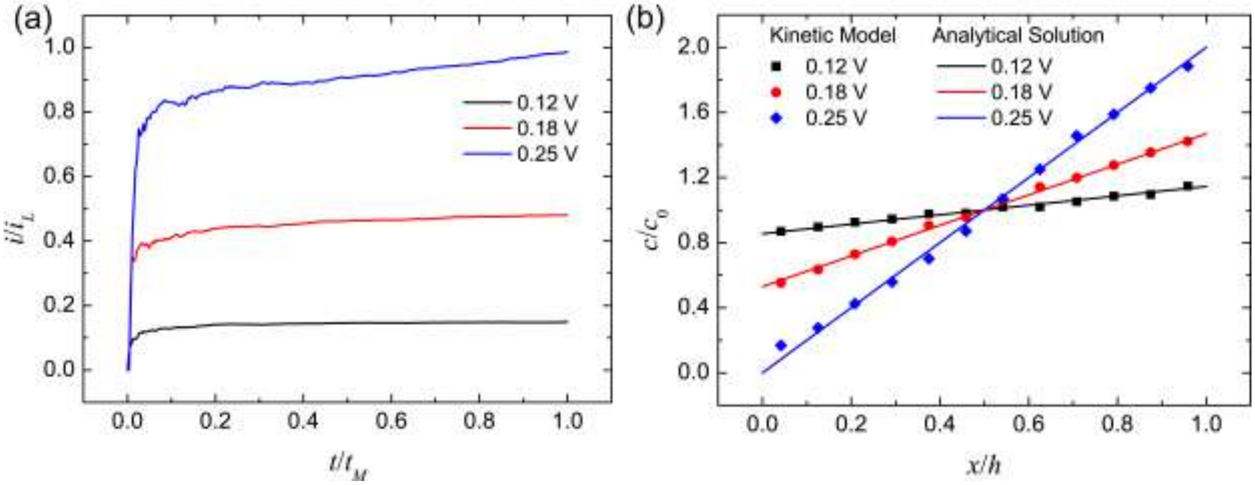

Figure 2. (a) Current density profiles at varying overpotentials. Here i_L and t_M are the limiting current density and total deposition time. The total deposition times are 1.03 s (0.12 V), 0.32 s (0.18 V), and 0.16 s (0.25 V). Corresponding to the three cases, Li-ion concentration profiles are shown in (b). Here, the lines are from the analytical solution and symbols correspond to the kinetic model.

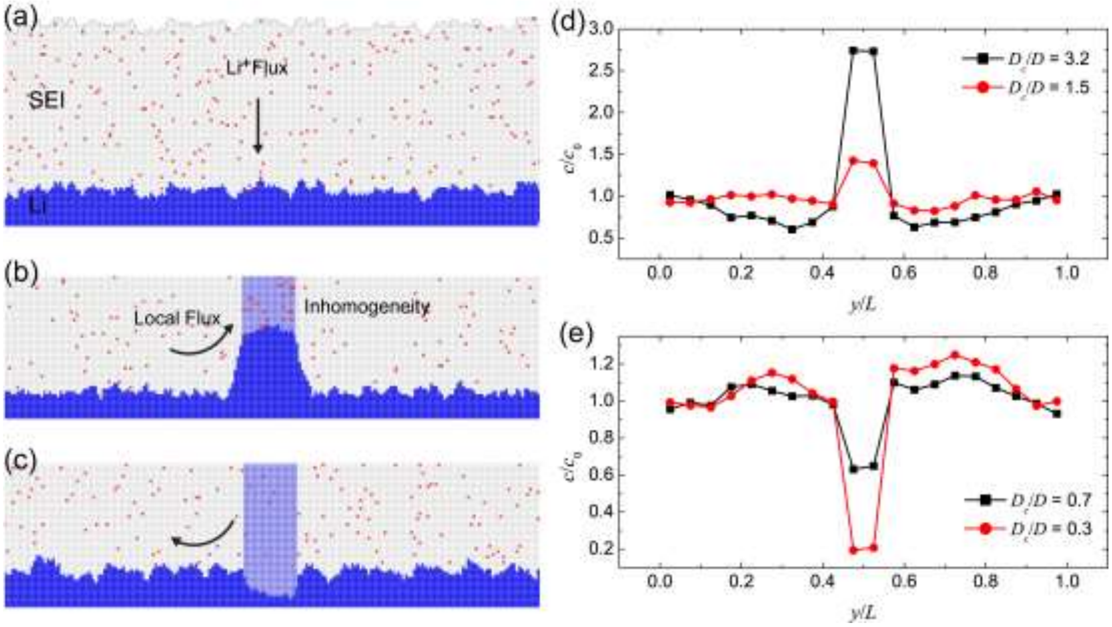

Figure 3. Effect of SEI inhomogeneity on Li electrodeposition. Here, the red circles are Li-ions and the blue circles are deposited Li atoms. Diffusion kinetics is varied in the center region, possessing a length of 0.1 *L* (*L* the system length) and a height of *h* (*h* is the SEI height). (a) Homogeneous SEI. (b) The center region has a lower diffusion barrier. (c) The center has a higher diffusion barrier. (d) and (e) are the concentration profiles in the SEI layer obtained from the kinetic model.

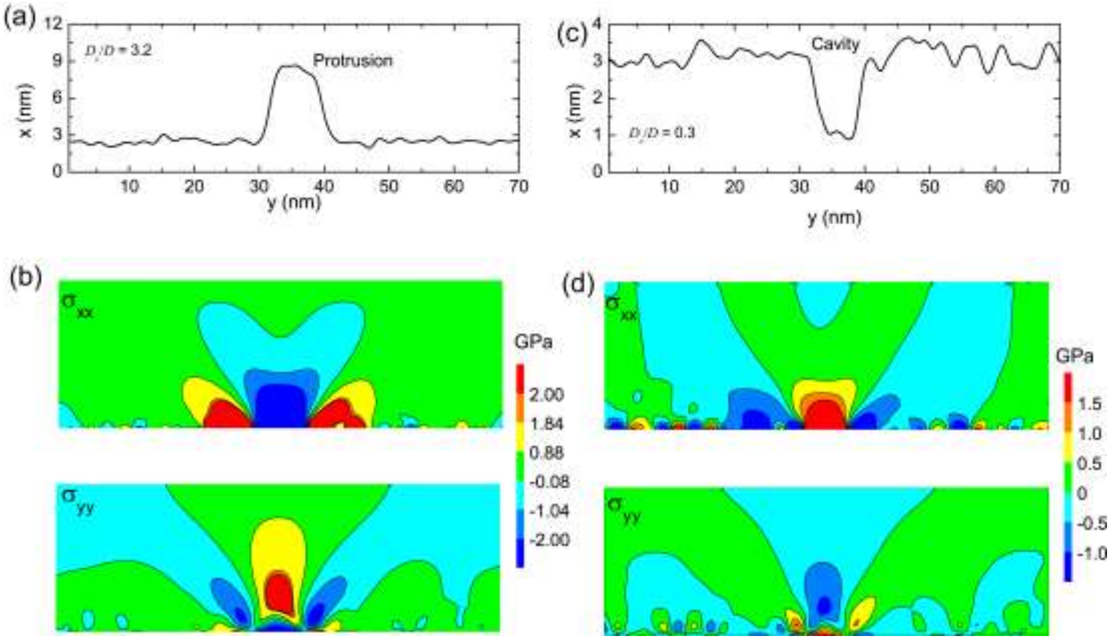

Figure 4. Nonuniform electrodeposition induced stress in the SEI layer. (a) Profile of the Li metal-SEI interface with $D_c/D = 3.2$, and (b) the corresponding stress contours $\left(\sigma_{xx}, \sigma_{yy}\right)$ in SEI. (c) Profile of the Li anode-SEI interface with $D_c/D = 0.3$, and (d) the corresponding stress contours $\left(\sigma_{xx}, \sigma_{yy}\right)$ in the SEI layer.

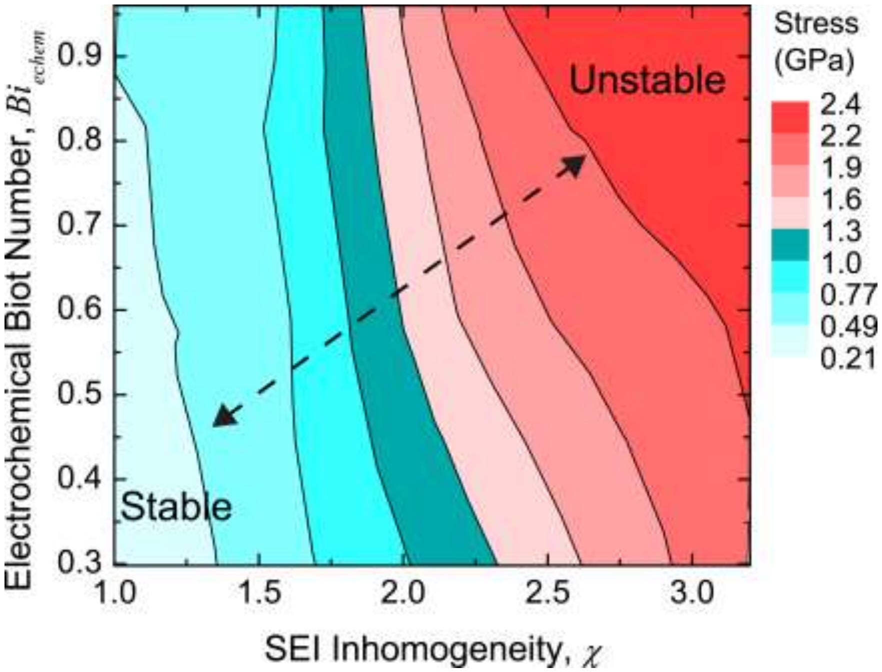

Figure 5. Phase map for maximum shear stress (Tresca failure criterion) as a function of electrochemical Biot number (Bi_{echem}) and SEI heterogeneity (χ). Maximum stress scales strongly with SEI inhomogeneity and shows mild increase with current density causing SEI fracture.

Graphical abstract

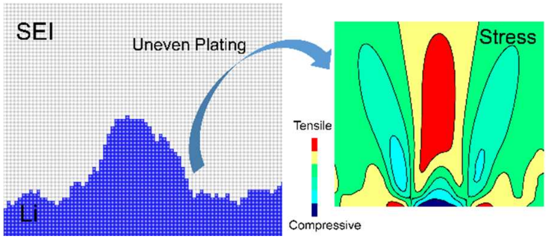

Coupled mechanism of nonuniform Li plating and interfacial stress induced SEI instability is elucidated.